PCCP

Reaction Mechanism and Dynamics for C8-hydroxylation of 9-Methylguanine Radical Cation by Water Molecules

Journal:	*Physical Chemistry Chemical Physics*
Manuscript ID	CP-ART-08-2021-003884.R1
Article Type:	Paper
Date Submitted by the Author:	15-Oct-2021
Complete List of Authors:	Zhou, Wenjing; Queens College of the City University of New York, Chemistry and Biochemistry Liu, Jianbo; Queens College of the City University of New York, Chemistry and Biochemistry

Reaction Mechanism and Dynamics for C8-hydroxylation of 9-Methylguanine Radical Cation by Water Molecules

Wenjing Zhou[a,b] and Jianbo Liu*[a,b]
[a] Department of Chemistry and Biochemistry, Queens College of the City University of New York, 65-30 Kissena Blvd., Queens, NY 11367, USA; [b] Ph.D. Program in Chemistry, The Graduate Center of the City University of New York, 365 5th Ave., New York, NY 10016, USA

Abstract In contrast to their spontaneous deprotonation in aqueous solution, reactions of guanine and guanosine radical cations with water in the gas phase are exclusively initiated by hydration of the radical cations as reported in a recent work (Sun *et al.*; *PCCP*, 2018, **20**, 27510). As gas-phase hydration reactions closely mimic the actual scenario for guanine radical cations in double-stranded DNA, exploration of subsequent reactions within their water complexes can provide an insight into the resulting oxidative damage to nucleosides. Herein guided-ion beam mass spectrometry experiment and direct dynamics trajectory simulations were carried out to examine prototype complexes of 9-methylguanine radical cation with one and two water ligands (*i.e.*, $9MG^{\bullet+}\cdot(H_2O)_{1\text{-}2}$) in the gas phase, wherein the complexes were activated by collisional activation in the experiment and by thermal excitation at high temperatures in the simulations. Guided by mass spectroscopic measurements, trajectory results and reaction potential energy surface, three reaction pathways were identified. The first two reaction pathways start with H-atom abstraction from water by the O6 and N7 atoms in $9MG^{\bullet+}$ and are referred to as HA_{O6} and HA_{N7}, respectively. The primary products of HA_{O6} and HA_{N7} reactions, including $[9MG + H_{O6}]^+$/$[9MG + H_{N7}]^+$ and $^{\bullet}OH$, react further to either form $[8OH\text{-}9MG + H_{O6}]^{\bullet+}$ and $[8OH\text{-}9MG + H_{N7}]^{\bullet+}$ via C8-hydroxylation or form radical cations of 6-*enol*-guanine (6-*enol*-$G^{\bullet+}$) and 7H-guanine ($7HG^{\bullet+}$) via S_N2-type methanol elimination. The third reaction pathway corresponds to the formation of $8OH\text{-}9MG^+$ by H elimination from the complex, referred to as HE. Among these product channels, $[8OH\text{-}9MG + H_{N7}]^{\bullet+}$ has the most favorable formation probability, especially in the presence of additional water molecules. This product may serve as a preceding structure to the 8-oxo-7,8-dihydroguanine lesion in DNA and has implications for health effects of radiation exposure and radiation therapy.

*E-mail: jianbo.liu@qc.cuny.edu. Tel: 1-718-997-3271.

I. Introduction

Guanosine has the lowest oxidation potential ($E°$) among the four DNA nucleosides. $E°$ measured with respect to the standard hydrogen electrode is 1.29 V for guanosine, 1.42 V for adenosine, 1.6 V for deoxycytidine and 1.7 V for thymidine.[1] The M06-2X theory predicted a similar order for the $E°$ of the constituent nucleobases: 1.40 V (guanine) < 1.75 V (adenine) < 2.00 V (thymine) < 2.18 V (cytosine).[2] In parallel with oxidation tendency, guanine has the lowest adiabatic ionization energy (AIE = 7.75 ± 0.05 eV),[3, 4] followed by adenine (8.267 ± 0.005 eV),[4, 5] cystine (8.66 ± 0.01 eV) [4, 5] and then thymine (8.82 ± 0.03 eV).[4, 6] Pairing guanine with cytosine in double-stranded (*ds*) DNA further decreases the $E°$ of guanine by 0.28 – 0.34 V[7, 8] and the AIE by 0.75 – 0.78 eV.[9, 10] These properties influence electron mobility within DNA[11] and lead to the formation of guanine radical cations ($G^{•+}$) as a trap[12] for oxidative damage to DNA upon ionizing radiation,[12, 13] photolysis,[14] chemical oxidation,[15] electron transfer in DNA-metal complexes,[16, 17] electrocatalytic oxidation[18, 19] and Type I photooxidation.[20, 21]

Guanine is a weak acid with pK_a of 9.2 – 9.6 for the nucleobase,[22] 9.4 for 2′-deoxyguanosine and 9.25 for guanosine.[13] But their pK_a decreases to 3.9 once they are ionized.[13,22] This creates a driving force for deprotonation of $G^{•+}$ at N1-proton[23] both in neutral aqueous solutions (within 56 ns)[24, 25] and in a low-temperature crystal state.[26, 27] Spectroscopy, kinetics and dynamics for the deprotonation of the $G^{•+}$ monomers[23, 28] and residues in oligonucleotides,[25, 29] single-,[30, 31] double-[24, 30, 31] and triple-stranded DNA[32] and G-quadruploe[33-35] as well as the secondary reactions[36, 37] of the resulting neutral radicals $[G - H]^{•}$ were examined by experiments and theoretical works. These studies discovered two distinctively different scenarios: free $G^{•+}$ monomers undergo spontaneous deprotonation prior to proceeding chemical reactions; in contrast, $G^{•+}$ residues in *ds*-DNA are stabilized through base pairing and the N1-proton (pK_a 3.9) of $G^{•+}$ is shared with the N3 (pK_a 4.3)[38] of cytosine via $G^{•+}{\cdot}C \rightleftharpoons [G - H_{N1}]^{•}{\cdot}[C + N_{H3}]^{+}$. The fate of $G^{•+}$ residues within *ds*-DNA are thus determined by their chemical reactions with water,[39] NO_2,[40] singlet O_2,[41] cross-linking with amino acids, etc.[42] These reactions lead to a variety of biological sequelae,[36, 43-45] most of which are mutagenic. An example is 8-oxo-7,8-dihydroguanine (abbreviated as OG).[20, 46, 47] OG

is the most common lesion observed in genomic, mitochondrial and telomeric DNA.[48] It marks oxidative stress within cells and tissues,[46, 49] and is implicated in photocleavage,[50] G·C → A·T mutation,[51] Alzheimer′s[52] and Parkinson′s diseases,[53] DNA-protein cross linking,[54, 55] etc.

OG may be produced through the hydration of $G^{\bullet+}$. This can be affirmed by the following two extremes: in *ss*-DNA, deprotonation of $G^{\bullet+}$ is 5 orders of magnitude faster than hydration.[29] As the deprotonation of N1-H reduces the feasibility of C8-hydroxylation,[47] little OG is produced;[56] in *ds*-DNA, hydration of $G^{\bullet+}$ instead becomes predominant and the ratio for OG formation in *ds*- *vs*. *ss*-DNA is 7 : 1.[31] Experimental studies of $G^{\bullet+}$ with water are mostly based on electron-transfer mediated photooxidation of DNA in oxygen-free solution,[20] ESR and electron nuclear double resonance measurements of $^{\bullet}OH$ addition to $[G + H_{N7}]^+$ (protonated at N7) in a crystal[57] and of $G^{\bullet+}$ hydration in DNA,[58] and time-resolved absorption spectroscopy measurement of $G^{\bullet+}$ hydration in DNA.[29] Augmented by computational modeling,[47, 59] an 8-hydroxy-7,8-dihydropurin-7-yl radical ($8OH\text{-}G^{\bullet}$)[12, 20] or its protonated counterpart $[8OH\text{-}G + H]^{\bullet+}$ was proposed as the most critical intermediate in the reaction of $G^{\bullet+}$ with H_2O, followed by its secondary oxidation to OG.[43, 60] However, a C8-hydroxyl intermediate had not been directly measured by mass spectrometry, and its formation mechanism, energetics and reaction dynamics are not fully understood.

In a previous gas-phase ion-molecule collision experiment,[39] we detected water-adducts of guanine- and guanosine-derived radical cations. The purpose of the present study is to reveal downstream conversion pathways and final products of the primary water complexes of guanine radical cations. To discover their probable reactions, these complexes were activated by collisional activation in a guided-ion beam experiment and by excitations at high temperatures in molecular dynamics simulations. The remainder of the paper is organized as follows. Section II reports the experimental results for the formation and collision-induced reactions of the water complexes with guanine and guanosine radical cations, mostly focusing on a model system which consists of 9-methylguanine radical cation ($9MG^{\bullet+}$) and water ligands. Section III describes direct dynamics simulations and electronic structure calculations.

Section IV reviews trajectory-predicted reaction intermediates and pathways for $9MG^{\bullet+}\cdot(H_2O)_{1\text{-}2}$, followed by the discussion of reaction potential energy surface (PES) leading from these intermediates to experimental products and the influence of additional water ligands. Conclusions and biological implications of the work are presented Section V.

II. Experimental Measurements and Results

1. Summary of Previous Results

In our previous work,[39] reactions of water with the radical cations of guanine ($9HG^{\bullet+}$), 9-methylguanine ($9MG^{\bullet+}$), 2′-deoxyguanosine ($dGuo^{\bullet+}$) and guanosine ($Guo^{\bullet+}$) were measured using ion-molecule scattering coupled with tandem mass spectrometry. Relevant findings are summarized below:

1) For all reactant radical cations, formation of an ion-water adduct represents the most favorable product channel. This channel dominates at low collision energies (E_{col}), but declines at high E_{col} due to short complex lifetime. Figure 1 presents the formation probabilities of different complex structures in the ion-molecule collisions of $9MG^{\bullet+}$ with H_2O, simulated using direct dynamics under experimental conditions. The water binding sites in each complex are specified by the last two numbers in its notation. Besides hydrogen-bonded (*i.e.*, $9MG^{\bullet+}$·W12a, $9MG^{\bullet+}$·W16 and $9MG^{\bullet+}$·W2b) and ion-dipole (*i.e.*, $9MG^{\bullet+}$·W8) complexes, a precursor complex was identified. The average complex lifetime is 1 μs at E_{col} = 0.1 eV. Among these complex structures, the precursor is dynamically unique with floppy complexation and no well-defined geometry or directional hydrogen bonds. The precursor has large-amplitude intermolecular motion, and thus allows repeated bimolecular encounters and increases the probability of locking into a reactive orientation.

2) Hydrogen elimination (HE) products were also detected in the water reactions with $9HG^{\bullet+}$, $9MG^{\bullet+}$, $dGuo^{\bullet+}$ and $Guo^{\bullet+}$, resulting in C8-hydroxylation of radical cations. The HE product yield increases at high E_{col}, which is consistent with the calculated reaction endothermicity.

2. New Measurements

To explore the chemical fate of the water adducts of guanine radical cations, the present work has

investigated their downstream reaction dynamics and product ions upon collisional activation. $9MG^{\bullet+}$ was used as a model nucleoside wherein the N9-methyl group mimics the attachment of a sugar group to nucleobase. It was verified in our experiments[39, 41] that $9MG^{\bullet+}$ resembles $dGuo^{\bullet+}$ and $Guo^{\bullet+}$ in terms of the charge and spin density distributions and the chemical reactivities of the guanine moiety.

Experiment was conducted on a home-built guided-ion beam tandem mass spectrometer coupled with an electrospray ionization (ESI) source.[61] Instrumentation and experimental details are available in the Supporting Information. In brief, the ion beam of $9MG^{\bullet+}\cdot H_2O$ was generated by ESI of a 2:1 methanol/water solution containing 0.5 mM 9MG and 0.25 mM $Cu(NO_3)_2$, in which the $[Cu^{II}(9MG)_3]^{\bullet2+}$ complex formed in electrospray underwent redox separation in the source chamber of the mass spectrometer,[62, 63] leading to $[Cu^{I}(9MG)_2]^{+}$ and $9MG^{\bullet+}$ (both in the presence and absence of water ligands).[39] Radical cations were thermalized to room temperature in a hexapole ion guide, followed by mass selection of $9MG^{\bullet+}\cdot H_2O$ (*m/z* 183) in a quadrupole mass filter. The mass-selected $9MG^{\bullet+}\cdot H_2O$ was subjected to collision with the Xe gas within a scattering cell that surrounds an octopole ion guide.

Collisional activation and reactions of $9MG^{\bullet+}\cdot H_2O$ were realized in two steps: $9MG^{\bullet+}\cdot H_2O + Xe \rightarrow 9MG^{\bullet+}\cdot H_2O\cdot Xe$ (a transient collision complex) $\xrightarrow{-Xe}$ $[9MG^{\bullet+}\cdot H_2O]^*$ (rovibrationally excited), followed by unimolecular reactions of $[9MG^{\bullet+}\cdot H_2O]^*$. The Xe atom has large mass and high polarizability, allowing for efficient translational-to-internal energy transfer ($T \rightarrow E_{internal}$) in $[9MG^{\bullet+}\cdot H_2O]^*$.[64-66] Product ions of collision-induced dissociation and reactions were analyzed by a second quadrupole mass filter and counted by an electron multiplier. Reaction was measured at different center-of-mass E_{col}. The scattering cell pressure was maintained at 0.015 mTorr. Under this condition, $9MG^{\bullet+}\cdot H_2O$ collided with the Xe gas only once or not all, so absolute product ion cross sections and reaction energy dependence was determined in a thin-target limit (analogous to the Beer-Lambert Law).[65]

A product ion mass spectrum of $9MG^{\bullet+}\cdot H_2O$ is demonstrated in Figure 2a. Collision-induced reactions produced three different product ions: product ions at *m/z* 165 correspond to elimination of a water ligand from reactant ions, product ions at *m/z* 166 represent the formation of protonated [9MG +

H]$^+$ via hydrogen abstraction from water, and those at *m/z* 151 correspond to the formation of 7H-guanine radical cation (7HG$^{\bullet+}$) and 6-*enol*-guanine radical cation (6-*enol*-G$^{\bullet+}$) via methanol elimination as discussed below. Individual product ion cross sections were measured as a function of E_{col} from 0.05 to 4.0 eV. Results are presented in Figure 2b – d, where error bars were estimated from 5 sets of measurement under the same conditions.

The cross section of 9MG$^{\bullet+}$ (*m/z* 165) has already raised from zero at the lowest E_{col}. This agrees with the fact that the water elimination energy of various 9MG$^{\bullet+}$·H_2O structures ranges from 0.4 to 0.68 eV (see hydration energies in Figure 1). The water-elimination energy is thus within the combined energy width of the 9MG$^{\bullet+}$·H_2O ion beam kinetic energy broadening (0.7 eV) and the ion internal energy (average 0.35 eV at 298 K). As a result, even at the lowest E_{col}, a significant fraction of the 9MG$^{\bullet+}$·H_2O reactant ions has sufficient energy to eliminate the water ligand.

Hydrogen abstraction (product ion *m/z* 166) and methanol elimination (*m/z* 151) reactions, on the other hand, have shown onsets at low E_{col} range. Due to the reactant ion beam kinetic energy spread and internal energy, their cross sections raised from zero before true reaction threshold energies (E_0). To extract E_0 values for the two reactions, each experimental cross section was fit to an intrinsic cross section function $\sigma(E_{col}) = \sigma_0 \frac{(E_{col} + E_{vib} + E_{rot} - E_0)^2}{E_{col}}$. $\sigma(E_{col})$ is assumed on the basis of a modified Line-of-Centers model,[64, 67-69] where σ_0 is an energy-independent fitting parameter, E_{vib} and E_{rot} are reactant vibrational and rotational energies, and E_0 is the dissociation threshold. $\sigma(E_{col})$ needs to be convoluted with the ion beam energy broadening.[70, 71] To this end, a Monte Carlo program[72] was used to sample 100000 collisions of 9MG$^{\bullet+}$·H_2O with Xe at each E_{col} under experimental conditions. The distributions of ion and gas velocities and ion E_{vib} and E_{rot} resulting from the Monte Carlo simulations were then fed into the LOC fitting. To take into account the kinetic shift (*i.e.*, E_{col} in excess of true E_0 is required to produce products from a reaction intermediate complex within the mass spectrometer detection time), Rice-Ramsperger-Kassel-Marcus (RRKM) model[73] was included in the fitting to decide whether each collision led to a detectable product ion or not. A leveling-off collision energy was used in the fitting so that $\sigma(E_{col})$ would

reach a plateau at high E_{col}. E_0 was adjusted in the fitting until the convoluted $\sigma(E_{col})$ matched the experimental data.

Note that the 9MG$^{\bullet+}$·H_2O ion beam consists of various conformers with different energies as illustrated in Figure 1. For example, the precursor and 9MG$^{\bullet+}$·W12a differ in energy by 0.28 eV. Therefore, the cross-section fitting was to only provide an average threshold energy for each product ion channel. The fitting results are plotted as red lines in Figures 2c – d, each of which reveals two separate product components. The product ions of *m/z* 166 consist of one contribution with E_0 = 1.1 eV and the other with E_0 = 1.4 eV with a branching ratio of 0.45 : 0.55; because the two thresholds are close to each other, it was also possible to fit the cross section using an average E_0 = 1.2 ± 0.2 eV. The product ions of *m/z* 155 have the first component with E_0 = 1.8 eV and the second one with E_0 = 3.0 eV.

3. Key Questions from the Experiment

The combination of the previous ion-molecule scattering experiment of 9MG$^{\bullet+}$ with H_2O and the present collision-induced reaction experiment of the 9MG$^{\bullet+}$·H_2O complex reveals two mechanistic regimes. The low energy regime is governed by the formation of a set of water complexes. The high energy regime results in three different downstream product ions from the water complexes: formation of $[9MG + H]^+$ accompanying $^{\bullet}$OH elimination, C8-hydroxylation accompanying H elimination, and formation of 7HG$^{\bullet+}$/6-*enol*-G$^{\bullet+}$ accompanying CH_3OH elimination. No radical cation deprotonation was seen at E_{col} up to 2.0 eV, as the proton transfer to water from the guanine N1, exocyclic N2a and N2b, and N9 is endothermic by 2.81, 2.64, 2.86 and 2.73 eV, respectively, per the ωB97XD/6-31+G(d,p) calculations.[39] Following the experiments, three key questions have arisen on which computational modeling may be able to shed light: (1) what are the mechanisms and dynamics for hydrogen abstraction, methanol elimination and C8-hydroxylation of 9MG$^{\bullet+}$·H_2O? (2) what is the most probable pathway leading to ultimate OG lesion? and (3) what are the effects of additional water molecules on reaction thermodynamics and kinetics?

III. Computational Methods

1. Dynamics Simulations

Direct dynamics trajectory simulations were used to mimic activated $9MG^{\bullet+}\cdot H_2O$ resulting from collisions with Xe, aimed at revealing probable reaction pathways and product structures of the complexes. To explore the effects of more than one explicit water ligand, we included both $9MG^{\bullet+}\cdot H_2O$ and $9MG^{\bullet+}\cdot(H_2O)_2$ in the computational modeling. Initial conditions for trajectories were set up using a chemical dynamics program Venus.[74, 75] Vibrational excitation of the reactants was sampled using the quantum Boltzmann probability distributions at a specific temperature,[76] *i.e.*, $P(n_i) = \exp\left(-\frac{n_i h\upsilon_i}{k_B T}\right)\left[1 - \exp\left(-\frac{h\upsilon_i}{k_B T}\right)\right]$ where ν_i and n_i are the vibrational frequency and quantum number of the i^{th} mode, and T is the simulation temperature. Quasi-classical vibrational states were simulated by giving individual reactant atoms displacements from equilibrium and momenta that are appropriate to the initial rovibrational state, with random phases for different modes. Reactant has zero-point energy (ZPE) in all vibrational modes. Reactant rotational energy (E_{rot}) was sampled from a classical Boltzmann distribution.

The Hessian-based predictor-corrector algorithm[77] implemented in Gaussian 09[78] was utilized to integrate classical equations of motion. Because the reaction time scale at a typical experimental temperature would be far too long for practical trajectory simulations (ion time-of-flight in the mass spectrometer is up to 500 μs), high simulation temperatures were used to accelerate and observe reactions on a reasonable time scale but not overwhelmingly dissociate reaction complexes or decompose the $9MG^{\bullet+}$ moiety in the trajectories. At high temperatures, trajectories may find reaction pathways with activation barriers too high to be relevant to the experimental condition. However, once enough trajectories have been collected with statistical meaningful results, all probable reaction pathways could be identified. Their reaction PESs were mapped out on the basis of the participating reaction intermediates, transition states (TSs) and products, and the pathways that are able to contribute significantly to the experiment could be singled out. Besides improving simulation efficiency, trajectories at high temperatures were able to explore multiple minima in the reactant conformational landscape and

on the reaction PES. Thus, all the various complex structures could form and contribute to trajectory outcomes, despite that the trajectories were initiated at a single precursor complex structure. This demonstrates the advantage of direct dynamics simulations that calculates energy, force constants and Hessians on the fly and allows molecules to show what reaction pathways and product structures are.

Trajectories were integrated with a step size of 0.25 $amu^{1/2}$·Bohr (corresponding to 0.4 fs each step in trajectory time), with the Hessian matrix updated every five steps. This step size was small enough for SCF convergence as well as to keep total energy and momentum conserved throughout the trajectory. Because millions of gradient and Hessian evaluation were required for each trajectory, a modest level of theory B3LYP/6-31G(d) was chosen. This method provided the similar calculation accuracy as B3LYP/6-31+G(d,p) but at a less computational cost. A quadratically convergent SCF method was opted in to integrate trajectory (*i.e.*, SCF = XQC)[79] in case the conventional first-order SCF algorithm failed to converge. Trajectories were terminated when the product separation exceeded 8 Å or the trajectory integration time reached 3 ps. gOpenMol[80] was used for trajectory visualization.

2. PES Calculations

Guided by trajectory results, the reactants, intermediates, TSs and products along probable reaction pathways were each fully optimized using two density functional theories (DFT): B3LYP and ωB97XD, each of which is paired with the 6-31+G(d,p) basis set. It was reported that the B3LYP-calculated redox properties of guanine are comparable to those obtained at CBS-QB3,[81] while ωB97XD can improve the orbital description of radical ions by mitigating self-interaction errors.[82] TSs were verified as first-order saddle points, and the vibrational mode associated with an imaginary frequency corresponds to the anticipated reaction pathway. Aside from local criterion, intrinsic reaction coordinate (IRC) calculation was carried out to verify reactant/product minima connected through each TS.

To examine possible spin contamination in the doublet-state PES, energies and T1-diagnostic[83, 84] of reaction structures were examined using the domain-based local pair-natural orbital coupled-cluster single-, double- and perturbative triple-excitation method[85] DLPNO-CCSD(T)/aug-cc-pVTZ. The

CCSD(T) theory can handle modest amounts of spin contamination in radicals (e.g., $<S^2> \leq 0.8$). Finally, as a sanity check, we explored reaction PES at the complete active space self-consistent field level CASSCF/6-31+G(d,p). The active spaces are (9,7) for $9MG^{\bullet+}$, (6,4) for H_2O, (16,11) for the $9MG^{\bullet+}\cdot H_2O$ reaction system, and (21,15) for the $9MG^{\bullet+}\cdot(H_2O)_2$ system. DFT and CASSCF calculations were carried out using Gaussian 09.[78] DLPNO-CCSD(T) calculations including $<S^2>$ and T1 diagnostic were accomplished using ORCA 4.2.[86]

IV. Computational Results and Discussion

1. Trajectories of $9MG^{\bullet+}\cdot H_2O$

We first simulated 100 trajectories of $9MG^{\bullet+}\cdot H_2O$ at a temperature of 600 K. This temperature was close to the vibrational temperature that the reactant ions gained in ion-molecule collisions at E_{col} = 1.0 eV. Nonetheless, none of the trajectories led to reactions. As rationalized previously, lack of reactions in the trajectories at the experimental temperature was not surprising as the simulation time was several orders of magnitude shorter than the ion detection time in the mass spectrometer. To enhance reaction efficiencies, we simulated 100 trajectories at 1200 K, 300 trajectories at 1800 K, and 100 trajectories at 3000 K. Less than 2% of the trajectories at 1200 K were reactive whereas most of the trajectories at 3000 K showed fragmentation of the 9MG moiety, rendering these two batches of trajectories useless for examining the chemistry of $9MG^{\bullet+}$ with water. The trajectories at 1800 K, on the other hand, have demonstrated a rich reaction chemistry. Reactive trajectories at 1800 K may be grouped into three different categories, as illustrated by representative trajectories shown in Figures 3 – 5 and videos in the Supporting Information. Each of them is discussed below.

1) Hydrogen abstraction from water by the N7 of $9MG^{\bullet+}$ (designated as HA_{N7} with the subscript indicating the reaction position at guanine). This pathway, with a trajectory reaction probability of 5 ± 1%, represents the most probable reaction mechanism. It leads to the formation of $[9MG + H_{N7}]^+$ and neutral $^{\bullet}OH$ radical. Figure 3 plots a representative HA_{N7} trajectory, in which the top frame plots the system potential energy (PE, along the left axis) and the center-of-mass (CM) separation (along the right

axis) between 9MG and water in the reactant and between $[9MG + H_{N7}]^+$ and $^\bullet OH$ in the product, and the bottom frame plots the breaking of a rH-OH bond in water and the formation of a new rN7-H bond in $[9MG + H_{N7}]^+$. Hydrogen abstraction occurs at 280 fs, as evidenced by the crossing over of rH-OH and rN7-H in the snapshot captured at that time. No obvious PE change was observed at the reaction moment, and the oscillation in PE is due to reactant/product E_{vib} including ZPE.

2) Hydrogen abstraction from water by the O6 of $9MG^{\bullet+}$ (designated as HA_{O6}). Analogous to HA_{N7}, this reaction produces a product pair of $[9MG + H_{O6}]^+$ and $^\bullet OH$. The trajectory probability for HA_{O6} is 3 ± 1%. A representative trajectory and a snapshot of HA_{O6} are illustrated in Figure 4. Both HA_{N7} and HA_{O6} may contribute to the *m/z* 166 product ions detected in the collision-induced reaction of $9MG^{\bullet+}\cdot H_2O$.

3) Hydrogen elimination (HE). This reaction pathway has the lowest trajectory probability (1 ± 0.5 %). It reproduces the HE product which we detected in the high-E_{col} collisions of guanine radical cations with water.[39] In a HE trajectory demonstrated in Figure 5, the CM separation refers to the distance between $9MG^{\bullet+}$ and water in the reactant and between $9MG^{\bullet+}$ and the hydroxyl group within the product. The reaction is initiated by water dissociation at 250 fs, followed by addition of $^\bullet OH$ to the C8 position in $9MG^{\bullet+}$ at 500 fs, forming $8OH\text{-}9MG^+$. The system PE increases upon water dissociation and then decreases upon the C8-OH addition.

2. Qualitative PES for $9MG^{\bullet+}\cdot H_2O$ Calculated at DFT Levels

Guided by the experimental and trajectory results, reaction coordinates of activated $9MG^{\bullet+}\cdot H_2O$ were mapped out using B3LYP/6-31+G(d,p), as shown in Figure 6. Structures for stationary points and TSs are depicted in ChemDraw schemes, and their Cartesian coordinates are available in the Supporting Information. To verify the B3LYP-predicted reaction schemes, we have reoptimized all reaction structures using ωB97XD/6-31+G(d,p). The two sets of DFT calculations are compared in Table 1. ωB97XD predicted the same reaction coordinates and product channels as B3LYP. The deviations between B3LYP and ωB97XD-calculated reaction energies are mostly within 0.2 eV. The DFT PES predicts that the reactions of activated $9MG^{\bullet+}\cdot H_2O$ may start with HA_{N7}, HA_{O6} and HE, as shown in

reactions (1 – 3):

$$9MG^{\bullet+} + H_2O \rightarrow \text{precursor} \xrightarrow{TS\_HA_{N7}} [9MG + H_{N7}]^+ (m/z\ 166) + {}^{\bullet}OH \quad (1)$$

$$9MG^{\bullet+} + H_2O \rightarrow \text{precursor} \xrightarrow{TS\_HA_{O6}} [9MG + H_{O6}]^+ (m/z\ 166) + {}^{\bullet}OH \quad (2)$$

$$9MG^{\bullet+} + H_2O \rightarrow \text{precursor} \xrightarrow{TS\_HE} [8\text{-OH-}9MG]^+ (m/z\ 182) + H \quad (3)$$

Note that the HE trajectory in Figure 5 shows sequential water dissociation and C8-hydroxylation. However, the static PES calculations resulted in only a synchronous step mediated by TS_HE; no sequential HE mechanism could be identified. This is because the time delay (250 fs) between water dissociation and C8-hydroxylation in the trajectory is comparable to the vibrational period of the TS_HE imaginary frequency, thus the two events may combine into a single reaction coordinate in TS_HE.

A puzzle in the analysis of trajectory results was that the experimentally detected methanol-elimination product channel was not reproduced in the trajectories. Note that the trajectory simulations focused on reactions that happen at the early stage within an activated $9MG^{\bullet+}\cdot H_2O$, consequently only primary products could be captured in the trajectories. It is reasonable to assume that the $[9MG + H]^+$ and ${}^{\bullet}OH$ produced in reactions (1) and (2) further react with each other. As depicted in Figure 6, each of $[9MG + H_{N7}]^+$ and $[9MG + H_{O6}]^+$ may follow two different reaction mechanisms with ${}^{\bullet}OH$. The first mechanism is featured by the attack of ${}^{\bullet}OH$ at the C8-position, leading to the formation of $[8OH\text{-}9MG + H_{N7}]^{\bullet+}$ and $[8OH\text{-}9MG + H_{O6}]^{\bullet+}$ as shown in reactions (4a) and (5a). The second mechanism is mediated by bimolecular nucleophilic substitution (S_N2)-type reaction, leading to methanol elimination and the formation of $7HG^{\bullet+}$ and 6-*enol*-$G^{\bullet+}$ as shown in reactions (4b) and (5b).

$$9MG^{\bullet+} + H_2O \rightarrow \text{precursor} \rightarrow [9MG + H_{N7}]^+ \cdots {}^{\bullet}OH \xrightarrow{TS\_8OH\_H_{N7}} [8OH\text{-}9MG + H_{N7}]^{\bullet+} \quad (4a)$$

$$9MG^{\bullet+} + H_2O \rightarrow \text{precursor} \rightarrow [9MG + H_{N7}]^+ \cdots {}^{\bullet}OH \xrightarrow{TS\_S_N2\_H_{N7}} 7HG^{\bullet+} + CH_3OH \quad (4b)$$

$$9MG^{\bullet+} + H_2O \rightarrow \text{precursor} \rightarrow [9MG + H_{O6}]^+ \cdots {}^{\bullet}OH \xrightarrow{TS\_8OH\_H_{O6}} [8OH\text{-}9MG + H_{O6}]^{\bullet+} \quad (5a)$$

$$9MG^{\bullet+} + H_2O \rightarrow \text{precursor} \rightarrow [9MG + H_{O6}]^+ \cdots {}^{\bullet}OH \xrightarrow{TS\_S_N2\_H_{O6}} 6\text{-}enol\text{-}G^{\bullet+} + CH_3OH \quad (5b)$$

The product ions $[8OH\text{-}9MG + H_{N7}]^{\bullet+}$ and $[8OH\text{-}9MG + H_{O6}]^{\bullet+}$ of reactions (4a) and (5a) have the same *m/z* (183) as the reactant complex $9MG^{\bullet+}\cdot H_2O$ and therefore could not be distinguished in product ion mass spectra. The product ions $7HG^{\bullet+}$ and 6-*enol*-$G^{\bullet+}$ of reactions (4b) and (5b), on the other hand, constituted the methanol-elimination products in the collision-induced experiment of $9MG^{\bullet+}\cdot H_2O$. The DFT-calculated trajectories and PES have thus rationalized all experimental product ions.

3. PES Refined by CASSCF and Comparison with Experiment

One concern in the DFT calculations is that spin contamination may not be well treated.[87] To clarify whether spin contamination brought about a severe consequence on DFT energies, we performed $\langle S^2 \rangle$ and T1 diagnostic for each reaction structure at DLPNO-CCSD(T)/aug-cc-pVTZ. Results of $\langle S^2 \rangle$ and T1 as well as the DLPNO-CCSD(T)-calculated reaction enthalpies were appended to Table 1. A pure doublet state is expected to have $\langle S^2 \rangle = 0.750$. According to the calculated $\langle S^2 \rangle$ values, most reaction structures seem to be not severely affected by spin contamination, with their maximum $\langle S^2 \rangle$ being 0.767. On the other hand, the T1 diagnostic of several reaction structures is close to or exceeds 0.02 (and occasionally 0.03), which implies an important multiconfigurational character for these species. We also found that the reaction structures of large T1 tend to show large differences between their DFT- and DLPNO-CCSD(T)-calculated energies, as can be seen in Table 1.

In view of the possible deficiencies of the DFT methods, we proceeded to explore reaction PES at the multi-reference CASSCF/6-31+G(d,p) level. The active spaces, as specified in computational methods, are sufficiently large to include the π and π^* orbitals (and the $\sigma_{N9\text{-}CH3}$ orbital in case of S_N2 reactions) of $9MG^{\bullet+}$ and the $\sigma_{O\text{-}H}$, $\sigma^*_{O\text{-}H}$ and $n_{O(2p)}$ orbitals of H_2O. The CASSCF reaction enthalpy was calculated on the basis of the electronic energy at CASSCF(15,11)/6-31+G(d,p) and the 298 K thermal correction at B3LYP/6-31+G(d,p), for which ZPE was scaled by a factor of 0.981.[88]

The performance of CASSCF *vs.* B3LYP can be comprehended in Figure 6, wherein energy differences between the two methods are indicated by green-colored gaps. On the one hand, the CASSCF-calculated PES reproduced the reaction coordinates predicted by B3LYP, and the CASSCF-

predicted SOMO orbitals are consistent with the B3LYP-calculated spin density distributions. On the other hand, compared to the B3LYP values for the same structures, the CASSCF energies decreases by an amount up to 1.0 eV, except that for $[8OH\text{-}9MG + H_{N7}]^{\bullet+}$ and $[8OH\text{-}9MG + H_{O6}]^{\bullet+}$ for which the energies increase by 0.2 – 0.25 eV.

According to the CASSCF PES, the most probable product channel corresponds to the formation of $[8OH\text{-}9MG + H_{N7}]^{\bullet+}$ via HA_{N7} in reaction (1), followed by the formation of $[8OH\text{-}9MG + H_{O6}]^{\bullet+}$ via HA_{O6} in reaction (2). To compare reactions (1) and (2) with the experimentally measured hydrogen abstraction threshold energy for $9MG^{\bullet+}\cdot H_2O$ (Figure 2c), we used the precursor structure of $9MG^{\bullet+}\cdot H_2O$ as the reaction starting point. With respect to the precursor complex, HA_{N7} has an activation barrier TS_HA_{N7} of 0.98 eV and product ($[9MG + H_{N7}]^+ + {}^{\bullet}OH$) endothermicity of 0.86 eV; HA_{O6} has an activation barrier TS_HA_{O6} of 0.89 eV and product ($[9MG + H_{O6}]^+ + {}^{\bullet}OH$) endothermicity of 1.31 eV, all of which are CASSCF values. Therefore, the CASSCF results predict E_0 = 0.98 eV (taken as the greater of rate-limiting barrier and product endothermicity) for HA_{N7} and 1.31 eV for HA_{O6}. The two LOC-fit E_0 values in Figure 2c (*i.e.*, 1.1 and 1.4 eV) have closely matched the threshold energies of HA_{N7} and HA_{O6} with respect to the precursor, suggesting the participation of both HA_{N7} and HA_{O6} in the experiment.

Reactions (4b) and (5b) account for methanol elimination of collisionally activated $9MG^{\bullet+}\cdot H_2O$. We have also fit the methanol-elimination cross section in Figure 2d using the LOC model, and found it is composed of two components with E_0 of 1.8 and 3.0 eV, respectively. The first E_0 is close to the energy gap between the activation barrier $TS\_S_N2\_H_{N7}$ (1.52 eV at CASSCF) and the precursor complex (-0.58 eV) in reaction (4b), and the second E_0 matches the gap between $TS\_S_N2\_H_{O6}$ (2.46 eV) and the precursor (-0.58 eV) in reaction (5b). This observation implies that reactions (4b) and (5b) have both contributed to product ions of *m/z* 151 in the experiment.

Despite the incapability of verifying reactions (4a) and (5a) in the experiment due to *m/z* coincidence between reactant and product ions, the formation of their products $[8OH\text{-}9MG + H_{N7}]^{\bullet+}$ and $[8OH\text{-}9MG + H_{O6}]^{\bullet+}$ can be inferred from two facts. First, the cross sections of reactions (4b) and (5b) are comparable

to those of reactions (1) and (2). This suggests that secondary reactions of $[9MG + H]^+$ with $^{\bullet}OH$ are significant in the experiment. Secondly, on the basis of reaction thermodynamics, reactions (4a) and (5a) should be more productive than reactions (4b) and (5b), suggesting that the yields of $[8OH\text{-}9MG + H_{N7}]^{\bullet+}$ and $[8OH\text{-}9MG + H_{O6}]^{\bullet+}$ should be higher than those of $7HG^{\bullet+}$ and 6-*enol*-$G^{\bullet+}$. Notably, reactions (4a) and (5a) represent critical steps to OG formation.

In the previous work,[39] we had calculated a concerted C8-OH addition mechanism, where the OH group of water attacks the C8-position of $9MG^{\bullet+}$ meanwhile the remaining H dissociates from the water and binds to the N7 of $9MG^{\bullet+}$, forming the same product $[8OH\text{-}9MG + H_{N7}]^{\bullet+}$ as that in reaction (4a). However, the activation barrier for synchronized additions is 0.52 eV higher than the two-step additions mediated by reactions (1) and (4a).

Finally, the HE reaction represents the most energy-demanding pathway with the activation barrier TS_HE of 2.36 eV and product endothermicity of 2.31 eV above the sum of $9MG^{\bullet+} + H_2O$. It emerges only at high energies, as verified in our previous experiment.[39]

Using the CASSCF results, we estimated the rate constants for HA_{N7}, HA_{O6} and HE using the TS-based RRKM theory[73] as $k = \frac{d\sum_{K=-J}^{J} G[E - E_0 - E_{rot}^{\dagger}(J,K)]}{h \sum_{K=-J}^{J} N[E - E_{rot}(J,K)]}$, where d is the reaction path degeneracy, G is the sum of accessible states from 0 to $E - E_0 - E_{\mathrm{rot}}^{\dagger}$ at individual TS, N is the activated complex′s density of states, E is the system energy, E_0 is the TS activation energy, E_{rot} and $E_{\mathrm{rot}}^{\dagger}$ are the rotational energies for the complex and the TS, J is the angular momentum quantum number, and K is the rotation quantum number. Calculations were done with the RRKM program of Zhu and Hase,[89] where $(2J + 1)$ K-levels were counted in k. At the trajectory simulation temperature 1800 K, $k(HA_{N7})$ is 8.15×10^9 s^{-1}, $k(HA_{O6})$ is 1.71×10^9 s^{-1} and k(HE) is 4.3×10^2 s^{-1}. The resulting branching ratio of HA_{N7} : HA_{O6} : HE is 0.83 : 0.17 : 0. The kinetics results qualitatively agree with the trajectory probabilities in that the HA_{N7} is the most favorable product channel, followed by HA_{O6}, whereas HE is negligible.

4. C8-OH Addition in the Presence of an Additional Water Ligand

Considering the importance of hydrogen abstraction in leading to C8-hydroxylation and ultimately the OG lesion in DNA and the fact that multiple water molecules may present around the DNA nucleobases in vivo, it warrants exploring reactions in the presence of an additional explicit water ligand. Figure 7 represents an inspiring water-assisted HA_{N7} trajectory in $9MG^{\bullet+}\cdot(H_2O)_2$ which was simulated at 1200 K. The top frame of Figure 7 shows the change of PE, and the middle and bottom frames show the changes of bond lengths in the water-assisted hydrogen abstraction: HA_{N7} between $9MG^{\bullet+}$ and one H_2O ligand occurs at 50 fs (shown in the middle frame); in the meantime, the second water transfers an H atom to the first water (shown in bottom frame).

An analogous water-assisted HA_{O6} trajectory is illustrated in Figure S1. The resulting reaction PES for the water-assisted HA_{N7} and HA_{O6} and subsequent C8-OH additions is manifested in Figure 8. Reaction energies are calculated at the B3LYP, ωB97XD, DLPNO-CCSD(T) and CASSCF levels of theory, and results are compiled in the second part of Table 1.

The RRKM kinetics modeling was carried out using the CASSCF PES of $9MG^{\bullet+}\cdot(H_2O)_2$. It was found that the values of $k(HA_{N7})$ and $k(HA_{O6})$ with the two water ligands are comparable to those with a single water. At room temperature, $k(HA_{N7})$ is 1.6×10^3 s^{-1} and $k(HA_{O6})$ is 5×10^3 s^{-1} for $9MG^{\bullet+}\cdot(H_2O)_2$. The most important change in the presence of an additional water is that the activation barriers for the C8-OH attack at $[9MG + H_{N7}]^+$ and $[9MG + H_{O6}]^+$ decrease significantly (by 0.53 – 0.65 eV) and thus are no long the rate-limiting steps. This observation has been affirmed at all four different levels of theory.

V. Conclusions

Reactions of the collisionally activated $9MG^{\bullet+}\cdot H_2O$ complexes were examined using guided-ion beam mass spectrometry. Their primary and secondary reaction mechanisms and dynamics were distinguished and delineated using direct dynamics simulations augmented by reaction PES. The primary reactions of $9MG^{\bullet+}\cdot H_2O$ are hydrogen abstraction from the water ligand by the N7 and O6 atom of $9MG^{\bullet+}$, forming $[9MG + H_{N7}]^+ + {}^{\bullet}OH$ and $[9MG + H_{O6}]^+ + {}^{\bullet}OH$, respectively. The secondary reactions of $[9MG + H_{N7}]^+$ and $[9MG + H_{O6}]^+$ with ${}^{\bullet}OH$ lead to C8-hydroxylation and methanol elimination. The computational

modeling not only reproduced experimental observations, but also identified low-energy formation pathways for [8OH-9MG + H_{N7}]$^{\bullet+}$ and [8OH-9MG + H_{O6}]$^{\bullet+}$. The biological importance of [8OH-9MG + H_{N7}]$^{+}$ and [8OH-9MG + H_{O6}]$^{+}$ is manifested by their link to the OG lesion in DNA and in the context of the current knowledge in the hydration *vs.* deprotonation of guanine radical cations. The guanine residues in *ds*-DNA are paired with complementary cytosine via Watson-Crick base pairing, in which the O6 atom of guanine is anchored to a O6(guanine)-H-N(cytosine) hydrogen bond.[70] On the other hand, the N7 atom of the guanine is located at the outer edge of the base pair and may be exposed to more water molecules. In this sense, formation of [8OH-9MG + H_{N7}]$^{\bullet+}$ is more biologically relevant.

Supporting Information

Instrumentation and experimental details, plots for water-assisted HA_{O6} trajectory, Cartesian coordinates for calculated structures, and trajectory videos.

Acknowledgment

This work was supported by the National Science Foundation (Grant No. CHE 1856362).

References

1 S. Steenken and S. V. Jovanovic, *J. Am. Chem. Soc.*, 1997, **119**, 617-618.
2 K. Lewis, K. Copeland and G. Hill, *Int. J. Quantum Chem.*, 2014, **114**, 1678-1684.
3 J. Zhou, O. Kostko, C. Nicolas, X. Tang, L. Belau, M. S. de Vries and M. Ahmed, *J. Phys. Chem. A*, 2009, **113**, 4829-4832.
4 M. Schwell and M. Hochlaf, *Top. Curr. Chem.*, 2015, **355**, 155-208.
5 D. Touboul, F. Gaie-Levrel, G. A. Garcia, L. Nahon, L. Poisson, M. Schwell and M. Hochlaf, *J. Chem. Phys.*, 2013, **138**, 094203.
6 H.-W. Jochims, M. Schwell, H. Baumgaertel and S. Leach, *Chem. Phys.*, 2005, **314**, 263-282.
7 T. Caruso, M. Carotenuto, E. Vasca and A. Peluso, *J. Am. Chem. Soc.*, 2005, **127**, 15040-15041.
8 C. E. Crespo-Hernández, D. M. Close, L. Gorb and J. Leszczynski, *J. Phys. Chem. B*, 2007, **111**, 5386-5395.
9 M. Hutter and T. Clark, *J. Am. Chem. Soc.*, 1996, **118**, 7574-7577.
10 H. M. Jaeger and H. F. Schaefer, III, *J. Phys. Chem. B*, 2009, **113**, 8142-8148.
11 F. D. Lewis, X. Liu, J. Liu, S. E. Miller, R. T. Hayes and M. R. Wasielewski, *Nature*, 2000, **406**, 51-53.
12 S. Steenken, *Chem. Rev.*, 1989, **89**, 503-520.
13 L. P. Candeias and S. Steenken, *J. Am. Chem. Soc.*, 1989, **111**, 1094-1099.
14 L. P. Candeias and S. Steenken, *J. Am. Chem. Soc.*, 1992, **114**, 699-704.
15 I. Saito, T. Nakamura and K. Nakatani, *J. Am. Chem. Soc.*, 2000, **122**, 3001-3006.
16 E. D. A. Stemp and J. K. Barton, *Met. Ions Biol. Syst.*, 1996, **33**, 325-365.
17 F. Tureček, *J. Phys. Chem. A*, 2021, **125**, 7090-7100.
18 H. H. Thorp, *Trends Biotechnol.*, 1998, **16**, 117-121.

19 C. Ribaut, G. Bordeau, P. Perio, K. Reybier, V. Sartor, O. Reynes, P.-L. Fabre and N. Chouini-Lalanne, *J. Phys. Chem. B*, 2014, **118**, 2360-2365.
20 H. Kasai, Z. Yamaizumi, M. Berger and J. Cadet, *J. Am. Chem. Soc.*, 1992, **114**, 9692-9694.
21 J. P. Hall, F. E. Poynton, P. M. Keane, S. P. Gurung, J. A. Brazier, D. J. Cardin, G. Winter, T. Gunnlaugsson, I. V. Sazanovich, M. Towrie, C. J. Cardin, J. M. Kelly and S. J. Quinn, *Nat. Chem.*, 2015, **7**, 961-967.
22 D. M. Close, *J. Phys. Chem. A*, 2013, **117**, 473-480.
23 A. Adhikary, A. Kumar, D. Becker and M. D. Sevilla, *J. Phys. Chem. B*, 2006, **110**, 24171-24180.
24 K. Kobayashi and S. Tagawa, *J. Am. Chem. Soc.*, 2003, **125**, 10213-10218.
25 K. Kobayashi, R. Yamagami and S. Tagawa, *J. Phys. Chem. B*, 2008, **112**, 10752-10757.
26 B. Rakvin, J. N. Herak, K. Voit and J. Huettermann, *Radiat. Environ. Biophys.*, 1987, **26**, 1-12.
27 E. O. Hole, W. H. Nelson, D. M. Close and E. Sagstuen, *J. Chem. Phys.*, 1987, **86**, 5218-5219.
28 X. Zhang, J. Jie, D. Song and H. Su, *J. Phys. Chem. A*, 2020, **124**, 6076-6083.
29 Y. Rokhlenko, N. E. Geacintov and V. Shafirovich, *J. Am. Chem. Soc.*, 2012, **134**, 4955-4962.
30 K. Hildenbrand and D. Schulte-Frohlinde, *Free Radical Res. Commun.*, 1990, **11**, 195-206.
31 Y. Rokhlenko, J. Cadet, N. E. Geacintov and V. Shafirovich, *J. Am. Chem. Soc.*, 2014, **136**, 5956-5962.
32 Y. Wang, H. Zhao, Q. Zhou, X. Dai, K. Liu, D. Song and H. Su, *J. Phys. Chem. B*, 2019, **123**, 2853-2863.
33 L. Wu, K. Liu, J. Jie, D. Song and H. Su, *J. Am. Chem. Soc.*, 2015, **137**, 259-266.
34 T. J. Merta, N. E. Geacintov and V. Shafirovich, *Photochem. Photobiol.*, 2019, **95**, 244-251.
35 Y. Yang, H. Su, W. Fang, X. Chen and W. Yang, *Phys. Chem. Chem. Phys.*, 2018, **20**, 13598-13606.
36 J. Cadet, M. Berger, G. W. Buchko, P. C. Joshi, S. Raoul and J.-L. Ravanat, *J. Am. Chem. Soc.*, 1994, **116**, 7403-7404.
37 O. R. Alshykhly, A. M. Fleming and C. J. Burrows, *J. Org. Chem.*, 2015, **80**, 6996-7007.
38 J. A. Dean, *Lange's Handbook of Chemistry, Fifteenth Edition*, McGraw-Hill, New York, 1999.
39 Y. Sun, W. Zhou, M. M. Moe and J. Liu, *Phys. Chem. Chem. Phys.*, 2018, **20**, 27510-27522.
40 N. Liu, F. Ban and R. J. Boyd, *J. Phys. Chem. A*, 2006, **110**, 9908-9914.
41 Y. Sun, M. Tsai, M. M. Moe and J. Liu, *J. Phys. Chem. A*, 2021, **125**, 1564-1576.
42 Y. Uvaydov, N. E. Geacintov and V. Shafirovich, *Phys. Chem. Chem. Phys.*, 2014, **16**, 11729-11736.
43 J. Cadet, T. Douki and J.-L. Ravanat, *Acc. Chem. Res.*, 2008, **41**, 1075-1083.
44 W. L. Neeley and J. M. Essigmann, *Chem. Res. Toxicol.*, 2006, **19**, 491-505.
45 A. M. Fleming and C. J. Burrows, *Free Radic. Biol. Med.*, 2017, **107**, 35-52.
46 S. Boiteux and J. P. Radicella, *Biochimie*, 1999, **81**, 59-67.
47 J. Reynisson and S. Steenken, *Phys. Chem. Chem. Phys.*, 2002, **4**, 527-532.
48 J. Cadet and P. D. Mascio, in *Modified nucleosides: In biochemistry, biotechnology and medicine*, ed. P. Herdewijn, Wiley-VCH Verlag Gmbh & Co. KGaA, Weinheim, 2008, pp. 29-47.
49 H. Sies, *Oxidative Stress*, Academic Press, 1985.
50 B. Armitage, *Chem. Rev.*, 1998, **98**, 1171-1200.
51 S. D. Bruner, D. P. G. Norman and G. L. Verdine, *Nature*, 2000, **403**, 859-866.
52 M. A. Lovell and W. R. Markesbery, *Arch. Neurol.*, 2001, **58**, 392-396.
53 J. Zhang, G. Perry, M. A. Smith, D. Robertson, S. J. Olson, D. G. Graham and T. J. Montine, *Am. J. Pathol.*, 1999, **154**, 1423-1429.
54 R. P. Hickerson, C. L. Chepanoske, S. D. Williams, S. S. David and C. J. Burrows, *J. Am. Chem. Soc.*, 1999, **121**, 9901-9902.
55 X. Xu, J. G. Muller, Y. Ye and C. J. Burrows, *J. Am. Chem. Soc.*, 2008, **130**, 703-709.
56 T. Douki, S. Spinelli, J.-L. Ravanat and J. Cadet, *J. Chem. Soc., Perkin Trans. 2*, 1999, 1875-1880.
57 S. D. Wetmore, R. J. Boyd and L. A. Eriksson, *J. Phys. Chem. B*, 1998, **102**, 9332-9343.
58 L. I. Shukla, A. Adhikary, R. Pazdro, D. Becker and M. D. Sevilla, *Nucleic Acids Res.*, 2004, **32**, 6565-6574.

59 R. N. Barnett, A. Bongiorno, C. L. Cleveland, A. Joy, U. Landman and G. B. Schuster, *J. Am. Chem. Soc.*, 2006, **128**, 10795-10800.
60 L. P. Candeias and S. Steenken, *Chem. - Eur. J.*, 2000, **6**, 475-484.
61 Y. Fang and J. Liu, *J. Phys. Chem. A*, 2009, **113**, 11250-11261.
62 P. Cheng and D. K. Bohme, *J. Phys. Chem. B*, 2007, **111**, 11075-11082.
63 L. Feketeová, E. Yuriev, J. D. Orbell, G. N. Khairallah and R. A. J. O'Hair, *Int. J. Mass Spectrom.*, 2011, **304**, 74-82.
64 P. B. Armentrout, *Int. J. Mass Spectrom.*, 2000, **200**, 219-241.
65 P. B. Armentrout, *J. Am. Soc. Mass Spectrom.*, 2002, **13**, 419-434.
66 A. E. Thomas, S. D. Chambreau, N. D. Redeker, A. A. Esparza, E. Shafirovich, T. Ribbeck, J. A. P. Sprenger, M. Finze and G. L. Vaghjiani, *J. Phys. Chem. A* 2020, **124**, 864-874.
67 C. Rebick and R. D. Levine, *J. Chem. Phys.*, 1973, **58**, 3942-3952.
68 R. D. Levine and R. B. Bernstein, *Molecular Reaction Dynamics and Chemical Reactivity*, Oxford University Press, New York, 1987.
69 J. Liu, B. van Devener and S. L. Anderson, *J. Chem. Phys.*, 2002, **116**, 5530-5543.
70 Y. Sun, M. M. Moe and J. Liu, *Phys. Chem. Chem. Phys.*, 2020, **20**, 14875-14888.
71 M. m. Moe, J. Benny, Y. Sun and J. Liu, *Phys. Chem. Chem. Phys.*, 2021, **23**, 9365-9380.
72 M. B. Sowa-Resat, P. A. Hintz and S. L. Anderson, *J. Phys. Chem.*, 1995, **99**, 10736-10741.
73 R. A. Marcus, *J. Chem. Phys.*, 1952, **20**, 359-364.
74 X. Hu, W. L. Hase and T. Pirraglia, *J. Comput. Chem.*, 1991, **12**, 1014-1024.
75 W. L. Hase, K. Bolton, P. de Sainte Claire, R. J. Duchovic, X. Hu, A. Komornicki, G. Li, K. Lim, D. Lu, G. H. Peslherbe, K. Song, K. N. Swamy, S. R. Vande Linde, A. Varandas, H. Wang and R. J. Wolf, VENUS 99: A General Chemical Dynamics Computer Program, Texas Tech University Lubbock, TX, 1999.
76 G. H. Peslherbe, H. Wang and W. L. Hase, *Adv. Chem. Phys.*, 1999, **105**, 171-201.
77 V. Bakken, J. M. Millam and H. B. Schlegel, *J. Chem. Phys.*, 1999, **111**, 8773-8777.
78 M. J. Frisch, G. W. Trucks, H. B. Schlegel, G. E. Scuseria, M. A. Robb, J. R. Cheeseman, G. Scalmani, V. Barone, B. Mennucci, G. A. Petersson, H. Nakatsuji, M. Caricato, X. Li, H. P. Hratchian, A. F. Izmaylov, J. Bloino, G. Zheng, J. L. Sonnenberg, M. Hada, M. Ehara, K. Toyota, R. Fukuda, J. Hasegawa, M. Ishida, T. Nakajima, Y. Honda, O. Kitao, H. Nakai, T. Vreven, J. J. A. Montgomery, J. E. Peralta, F. Ogliaro, M. Bearpark, J. J. Heyd, E. Brothers, K. N. Kudin, V. N. Staroverov, T. Keith, R. Kobayashi, J. Normand, K. Raghavachari, A. Rendell, J. C. Burant, S. S. Iyengar, J. Tomasi, M. Cossi, N. Rega, J. M. Millam, M. Klene, J. E. Knox, J. B. Cross, V. Bakken, C. Adamo, J. Jaramillo, R. Gomperts, R. E. Stratmann, O. Yazyev, A. J. Austin, R. Cammi, C. Pomelli, J. W. Ochterski, R. L. Martin, K. Morokuma, V. G. Zakrzewski, G. A. Voth, P. Salvador, J. J. Dannenberg, S. Dapprich, A. D. Daniels, O. Farkas, J. B. Foresman, J. V. Ortiz, J. Cioslowski and D. J. Fox, Gaussian 09, Rev. D.01, Gaussian, Inc, Wallingford, CT, 2013.
79 G. B. Bacskay, *Chem. Phys.*, 1981, **61**, 385-404.
80 L. Laaksonen, gOpenMol, Center for Scientific Computing, Espoo, Finland, 3.0 edn., 2005, vol. 3.0, p. available at www.csc.fi/gopenmol/.
81 B. Thapa and H. B. Schlegel, *J. Phys. Chem. A*, 2015, **119**, 5134-5144.
82 A. Kumar and M. D. Sevilla, *J. Phys. Chem. B*, 2014, **118**, 5453-5458.
83 T. J. Lee and P. R. Taylor, *Int. J. Quantum Chem., Quantum Chem. Symp.*, 1989, **36**, 199-207.
84 D. Jayatilaka and T. J. Lee, *J. Chem. Phys.*, 1993, **98**, 9734-9747.
85 D. G. Liakos, M. Sparta, M. K. Kesharwani, J. M. L. Martin and F. Neese, *J. Chem. Theory Comput.*, 2015, **11**, 1525-1539.
86 F. Neese, *WIREs Comput Mol Sci*, 2018, **8**, e1327.
87 J. A. Pople, P. M. W. Gill and N. C. Handy, *Int. J. Quantum Chem.*, 1995, **56**, 303-305.
88 I. M. Alecu, J. Zheng, Y. Zhao and D. G. Truhlar, *J. Chem. Theory Comput.*, 2010, **6**, 2872-2887.
89 L. Zhu and W. L. Hase, A General RRKM Program (QCPE 644), Quantum Chemistry Program Exchange, Chemistry Department, University of Indiana, Bloomington, 1993.

Table 1 Relative enthalpies (eV, 298 K) of reaction species calculated at different levels of theory and their spin and T1 diagnostic

Species	B3LYP/ 6-31+G(d,p)	ωB97XD/ 6-31+G(d,p)	DLPNO-CCSD(T)/ aug-cc-pVTZ [a]	CASSCF/ 6-31+G(d,p) [a,b]	$<S^2>$ [c]	T1 diagnostic [c]
Reactions of $9MG^{\bullet+}\cdot H_2O$						
$9MG^{\bullet+} + H_2O$	0.0	0.0	0.0	0.0	0.7520	0.020 ($9MG^{\bullet+}$)
$9MG^{\bullet+}\cdot H_2O$ (precursor)	-0.38	-0.42	-0.37	-0.58	0.7518	0.019
TS_HA_{N7}	0.59	0.78	1.78	0.40	0.7522	0.021
$[9MG + H_{N7}]^{+}\cdots {}^{\bullet}OH$	0.51	0.43	0.48	0.16	0.7520	0.015
$[9MG + H_{N7}]^{+} + {}^{\bullet}OH$	1.00	0.96	0.96	0.28	0.7600	0.015 ($[9MG + H_{N7}]^{+}$)
$TS\_8OH\_H_{N7}$	0.83	0.84	0.92	0.46	0.7504	0.016
$[8OH\text{-}9MG + H_{N7}]^{\bullet+}$	-0.63	-0.85	-0.66	-0.38	0.7507	0.016
$TS\_\ S_N2\_H_{N7}$	2.52	2.87	3.61	1.52	0.7520	0.022
$7HG^{\bullet+} + CH_3OH$	0.63	0.77	0.78	-0.14	0.7516	0.021 ($7HG^{\bullet+}$)
TS_HA_{O6}	0.64	0.69	2.48	0.31	0.7525	0.035
$[9MG + H_{O6}]^{+}\cdots {}^{\bullet}OH$	0.69	0.68	0.77	0.64	0.7502	0.016
$[9MG + H_{O6}]^{+} + {}^{\bullet}OH$	1.30	1.28	1.21	0.73	0.757	0.014 ($[9MG + H_{O6}]^{+}$)
$TS\_8OH\_H_{O6}$	1.16	1.15	1.18	0.87	0.7511	0.016
$[8OH\text{-}9MG + H_{O6}]^{\bullet+}$	-0.03	-0.21	-0.12	0.17	0.7518	0.018
$TS\_\ S_N2\_H_{O6}$	3.06	3.30	3.41	2.46	0.7504	0.023
6-*enol*-$G^{\bullet+} + CH_3OH$	1.49	1.67	1.64	0.94	0.7522	0.025 (6-*enol*-$G^{\bullet+}$)
TS_HE	2.65	2.85	2.72	2.36	0.7501	0.015
$8OH\text{-}9MG^{+} + H$	2.32	2.19	2.06	2.31	0.7500	0.014(
Reactions of $9MG^{\bullet+}\cdot(H_2O)_2$						
$9MG^{\bullet+} + 2H_2O$	0.0	0.0	0.0	0.0	0.7520	0.020 ($9MG^{\bullet+}$)
$9MG^{\bullet+}\cdot(H_2O)_2$	-0.71	-0.79	-0.68	-0.91	0.7516	0.018
$TS(H_2O)\_HA_{N7}$	0.30	– [d]	1.44	0.47	0.7518	0.019
$[9MG + H_{N7}]^{+}\cdot H_2O\cdots {}^{\bullet}OH$	0.03	-0.11	0.02	-0.64	0.7501	0.014
$TS(H_2O)\_8OH\_H_{N7}$	0.13	0.06	0.23	-0.19	0.7504	0.015
$[8OH\text{-}9MG + H_{N7}]^{\bullet+}\cdot H_2O$	-1.21	-1.49	-1.23	-0.93	0.7506	0.015
$TS(H_2O)\_HA_{O6}$	0.07	0.03	– [d]	0.33	0.7666 [e]	0.019 [e]
$[9MG + H_{O6}]^{+}\cdot H_2O\cdots {}^{\bullet}OH$	0.13	0.08	– [d]	0.17	0.7563 [e]	0.016 [e]
$TS(H_2O)\_8OH\_H_{O6}$	0.33	0.27	0.40	0.34	0.7510	0.016
$[8OH\text{-}9MG + H_{O6}]^{\bullet+}\cdot H_2O$	-0.80	-1.05	-0.85	-0.35	0.7514	0.018

[a] Calculated using the B3LYP/6-31+G(d,p) optimized geometries.

[b] CASSCF(9,7)/6-31+G(d,p) was used for $9MG^{\bullet+}$, CASSCF(6,4)/6-31+G(d,p) for H_2O, CASSCF(15,11)/6-31+G(d,p) for $9MG^{\bullet+}\cdot H_2O$ reactions, and CASSCF(21,15)/6-31+G(d,p) for $9MG^{\bullet+}\cdot(H_2O)_2$ reactions.

[c] Calculated at DLPNO-CCSD(T)/aug-cc-pVTZ. $<S^2> = 0$ for H_2O and methanol.

[d] SCF calculation was not converged.

[e] $<S^2>$ and T1 diagnostic were obtained at CCSD(T)/6-31+G(d,p).

Figure Captions

Fig. 1 Formation of different $9MG^{\bullet+}\cdot H_2O$ complex structures in the collisions of $9MG^{\bullet+}$ with water. Distribution probabilities are based on 100 trajectories simulated for $9MG^{\bullet+} + H_2O$ at E_{col} = 0.1 eV. Hydration sites are indicated by the last two numbers in notations. Hydration energies ($\Delta H_{hydration}$, eV, with respect to starting reactants) were evaluated at DLPNO-CCSD(T)/aug-cc-pVTZ//ωB97XD/6-31+G(d,p) with 298 K thermal corrections.

Fig .2 (a) Product ion mass spectrum for collision-induced reactions of $9MG^{\bullet+}\cdot H_2O$ at E_{col} = 1.0 eV; and (b – d) cross sections of individual product ions as a function of E_{col}, where circled points are experimental data and red lines are LOC fits.

Fig. 3 A trajectory for hydrogen abstraction from water by the N7 of $9MG^{\bullet+}$, simulated at 1800 K using the B3LYP/6-31G(d) method. The top frame shows the changes of PE and reactant/product CM separation, and the bottom frame shows variations of reactive bond lengths. A trajectory video is provided in the Supporting Information.

Fig. 4 A trajectory for hydrogen abstraction from water by the O6 of $9MG^{\bullet+}$, simulated at 1800 K using the B3LYP/6-31G(d) method. The top frame shows the changes of PE and reactant/product CM separation, and the bottom frame shows variations of reactive bond. A trajectory video is provided in the Supporting Information.

Fig. 5 A trajectory for hydrogen elimination in $9MG^{\bullet+}\cdot H_2O$, simulated at 1800 K using the B3LYP/6-31G(d) method. The top frame shows the changes of PE and CM separation between the $9MG^{\bullet+}$ and water moieties in $9MG^{\bullet+}\cdot H_2O$ and between the $9MG^{\bullet+}$ moiety and 8-hydroxy group within $8OH\text{-}9MG^{+}$, and the bottom frame shows variations of reactive bond lengths. A trajectory video is provided in the Supporting Information.

Fig. 6 Reaction PES for $9MG^{\bullet+}\cdot H_2O$ calculated at B3LYP/6-31+G(d,p) and CASSCF(15,11)/6-31+G(d,p)//B3LYP/6-31+G(d,p), respectively. Reaction enthalpies (eV, with respect to separated $9MG^{\bullet+}$ and H_2O) were evaluated at 298 K.

Fig. 7 A trajectory for water-assisted HA_{N7} in $9MG^{\bullet+}\cdot(H_2O)_2$ simulated at 1200 K using the B3LYP/6-31G(d) method. The top frame shows the change of PE, and the middle and bottom frames show the variations of reactive bond lengths. A trajectory video is provided in the Supporting Information.

Fig. 8 Reaction PES of $9MG^{\bullet+}\cdot(H_2O)_2$ calculated at B3LYP/6-31+G(d,p) and CASSCF(21,15)/6-31+G(d,p)//B3LYP/6-31+G(d,p), respectively. Reaction enthalpies (eV, with respect to separated $9MG^{\bullet+}$ and two H_2O) were evaluated at 298 K.

Fig. 1

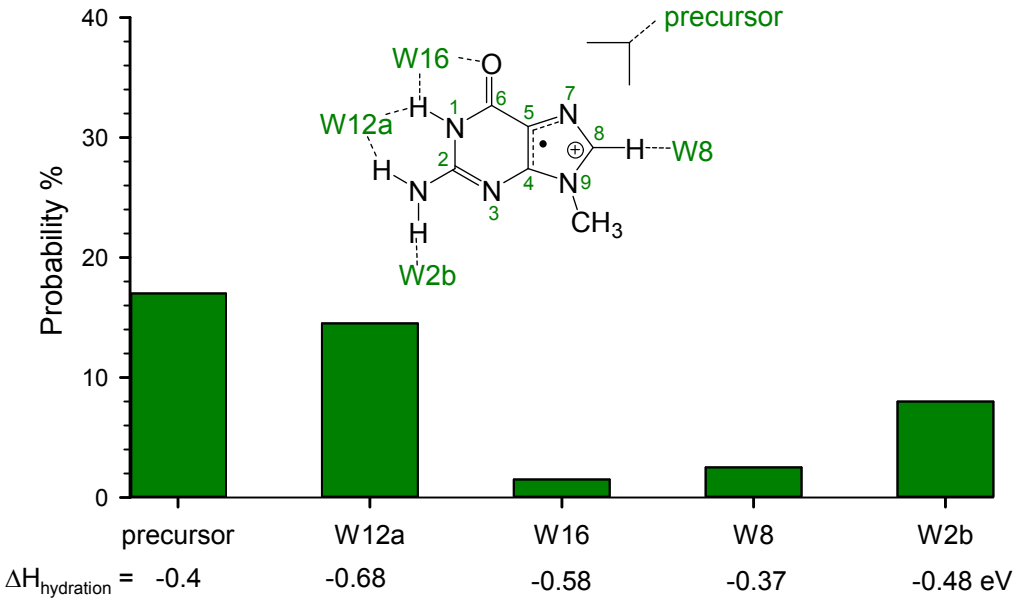
Probability %
40
30
20
10
0
precursor
W16
W12a
W8
W2b
O
H
N
CH3
1
2
3
4
5
6
7
8
9
precursor
W12a
W16
W8
W2b
ΔH hydration = -0.4
-0.68
-0.58
-0.37
-0.48 eV

Fig. 2

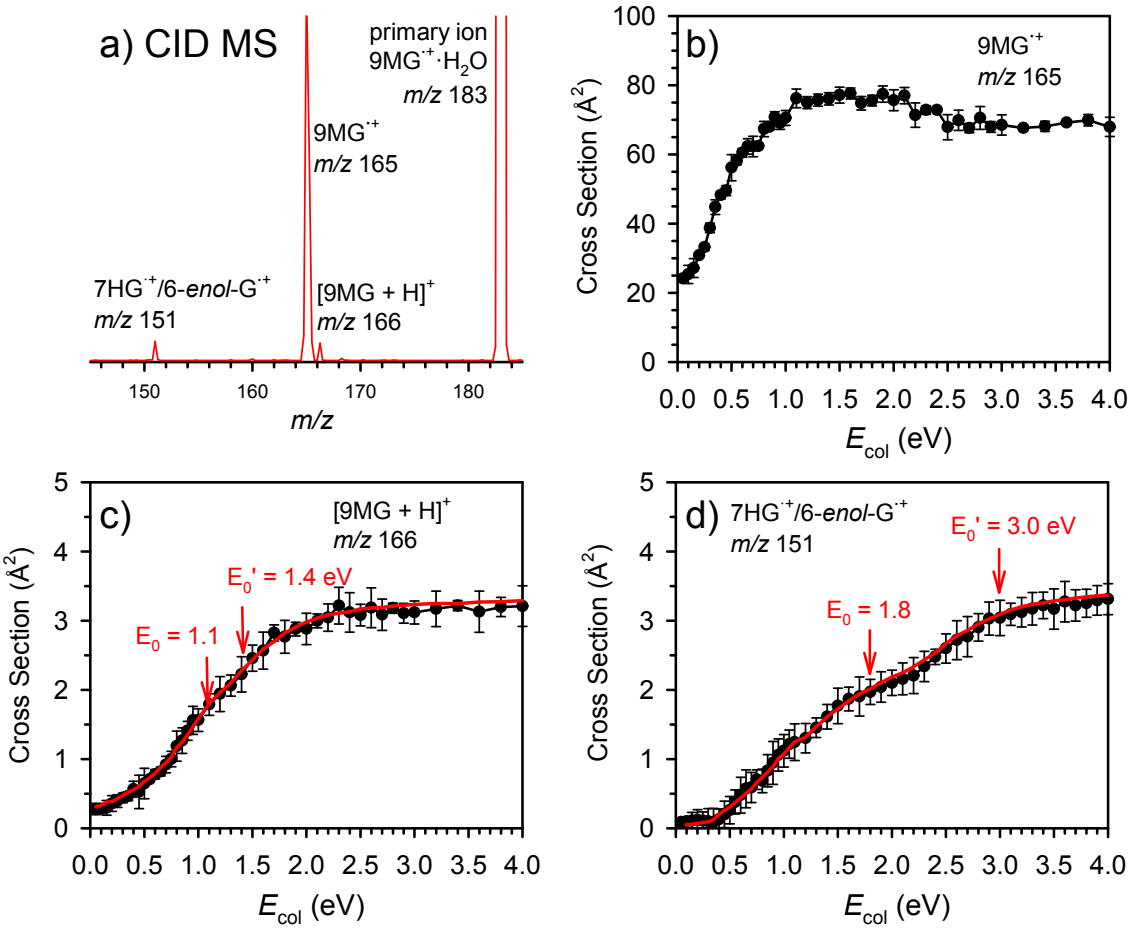
a) CID MS
primary ion
9MG$^{\cdot+}$·H$_2$O
m/z 183
9MG$^{\cdot+}$
m/z 165
7HG$^{\cdot+}$/6-*enol*-G$^{\cdot+}$
m/z 151
[9MG + H]$^+$
m/z 166
150 160 170 180
m/z
b)
9MG$^{\cdot+}$
m/z 165
Cross Section (Å^2)
0 20 40 60 80 100
0.0 0.5 1.0 1.5 2.0 2.5 3.0 3.5 4.0
E_{col} (eV)
c)
[9MG + H]$^+$
m/z 166
E$_0$' = 1.4 eV
E$_0$ = 1.1
Cross Section (Å^2)
0 1 2 3 4 5
0.0 0.5 1.0 1.5 2.0 2.5 3.0 3.5 4.0
E_{col} (eV)
d)
7HG$^{\cdot+}$/6-*enol*-G$^{\cdot+}$
m/z 151
E$_0$' = 3.0 eV
E$_0$ = 1.8
Cross Section (Å^2)
0 1 2 3 4 5
0.0 0.5 1.0 1.5 2.0 2.5 3.0 3.5 4.0
E_{col} (eV)

Fig. 3

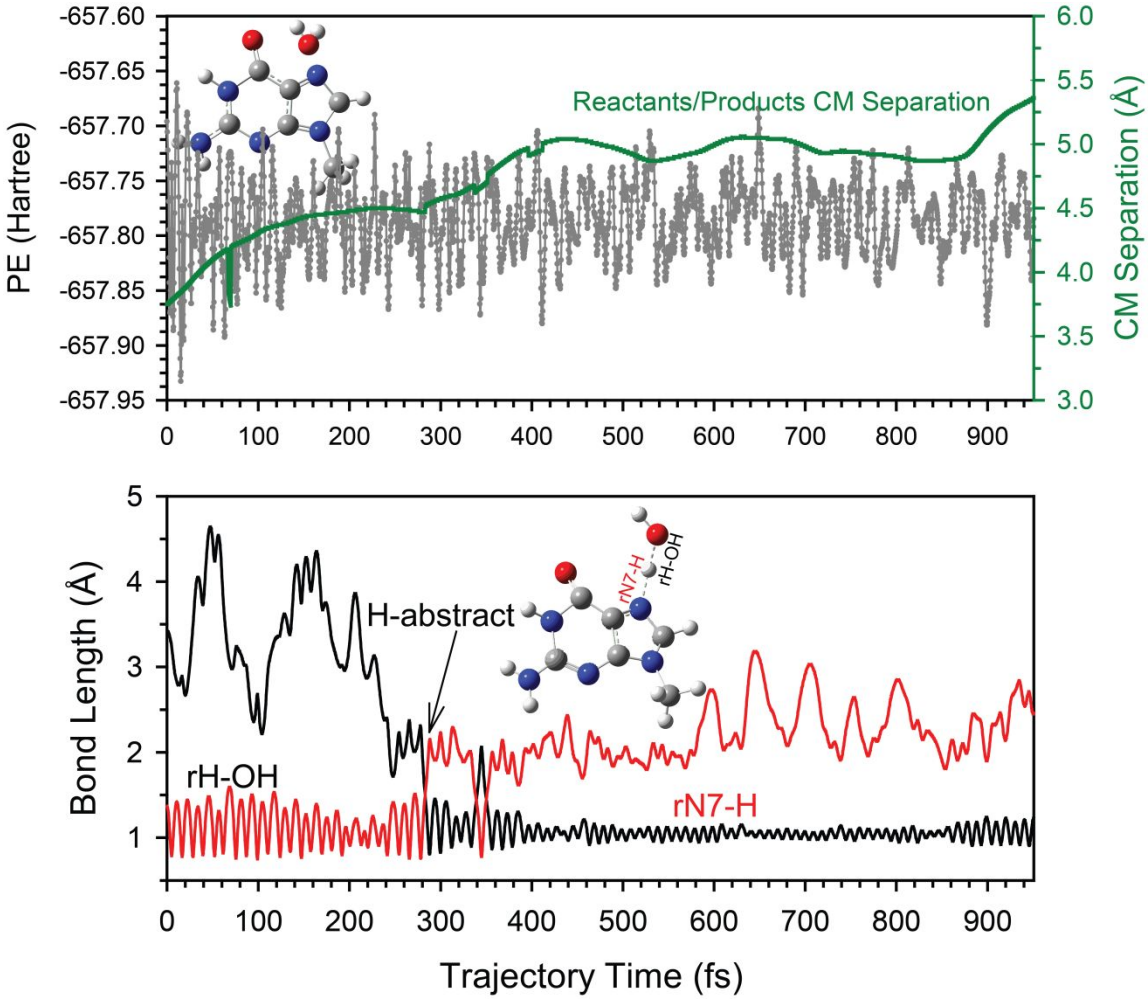
PE (Hartree)
-657.60
-657.65
-657.70
-657.75
-657.80
-657.85
-657.90
-657.95
Reactants/Products CM Separation
CM Separation (Å)
6.0
5.5
5.0
4.5
4.0
3.5
3.0
0
100
200
300
400
500
600
700
800
900
Bond Length (Å)
5
4
3
2
1
H-abstract
rH-OH
rN7-H
Trajectory Time (fs)

Fig. 4

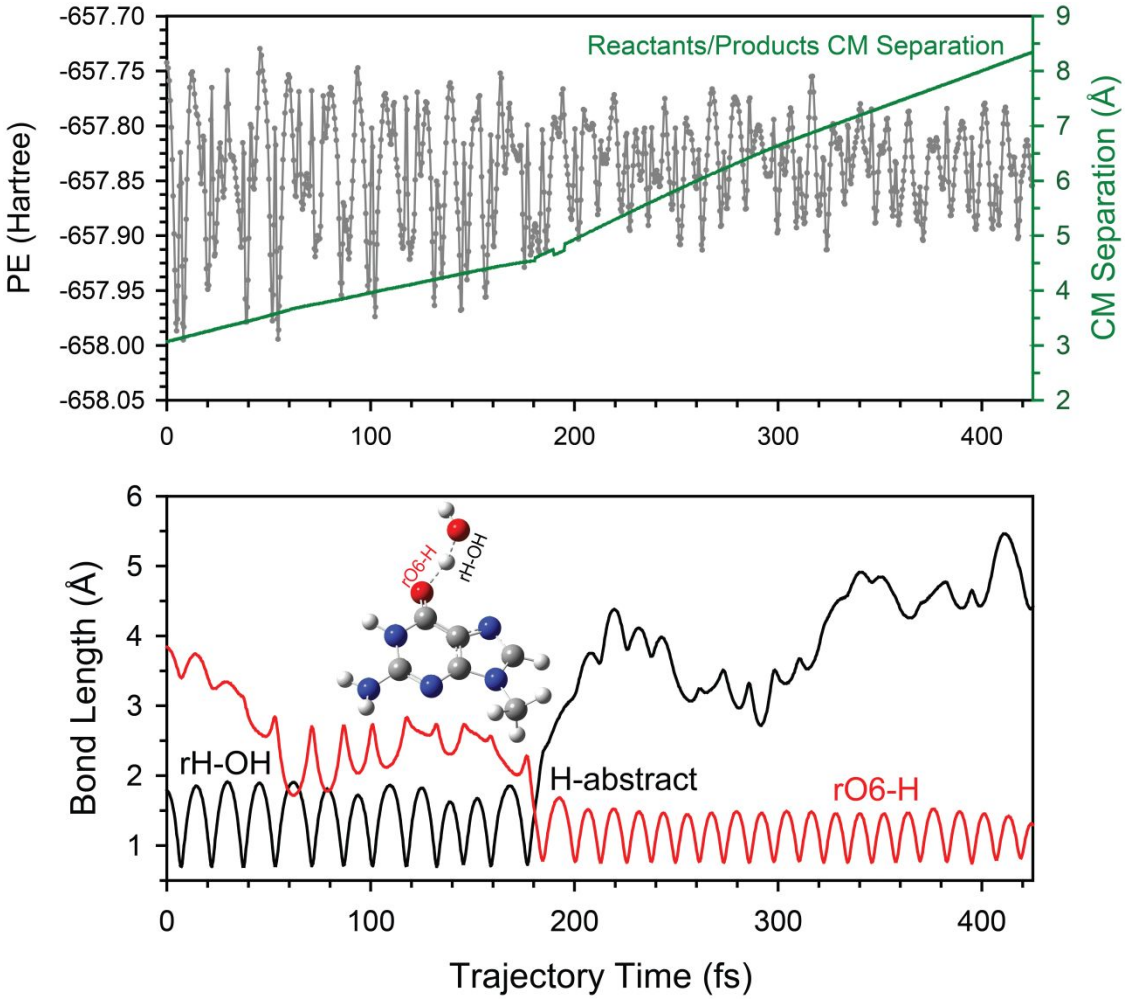
Reactants/Products CM Separation
PE (Hartree)
CM Separation (Å)
-657.70
-657.75
-657.80
-657.85
-657.90
-657.95
-658.00
-658.05
9
8
7
6
5
4
3
2
0
100
200
300
400
Bond Length (Å)
rO6-H
rH-OH
rH-OH
H-abstract
rO6-H
6
5
4
3
2
1
0
100
200
300
400
Trajectory Time (fs)

Fig. 5

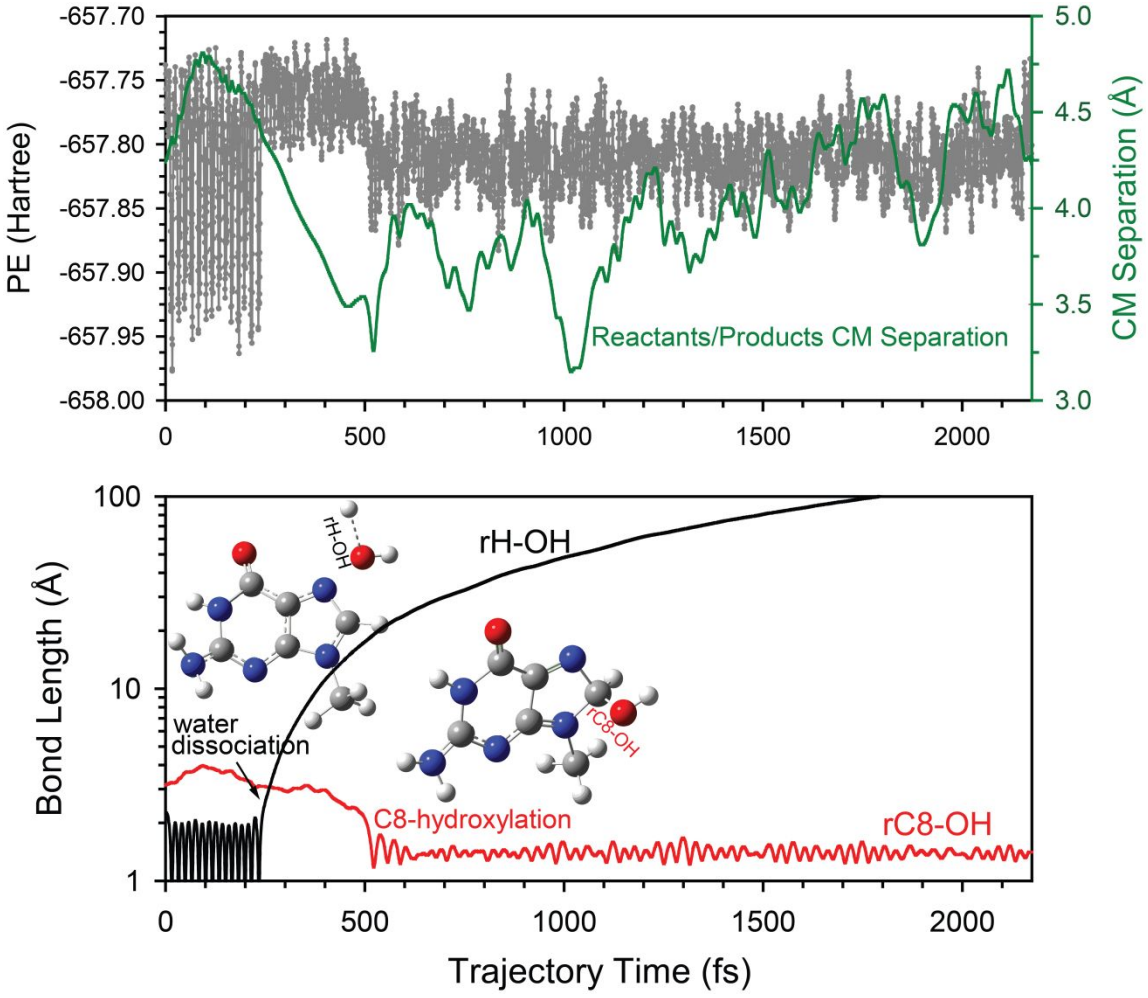
PE (Hartree)
-657.70
-657.75
-657.80
-657.85
-657.90
-657.95
-658.00
CM Separation (Å)
5.0
4.5
4.0
3.5
3.0
Reactants/Products CM Separation
0
500
1000
1500
2000
Bond Length (Å)
100
10
1
rH-OH
water
dissociation
C8-hydroxylation
rC8-OH
Trajectory Time (fs)

Fig. 6

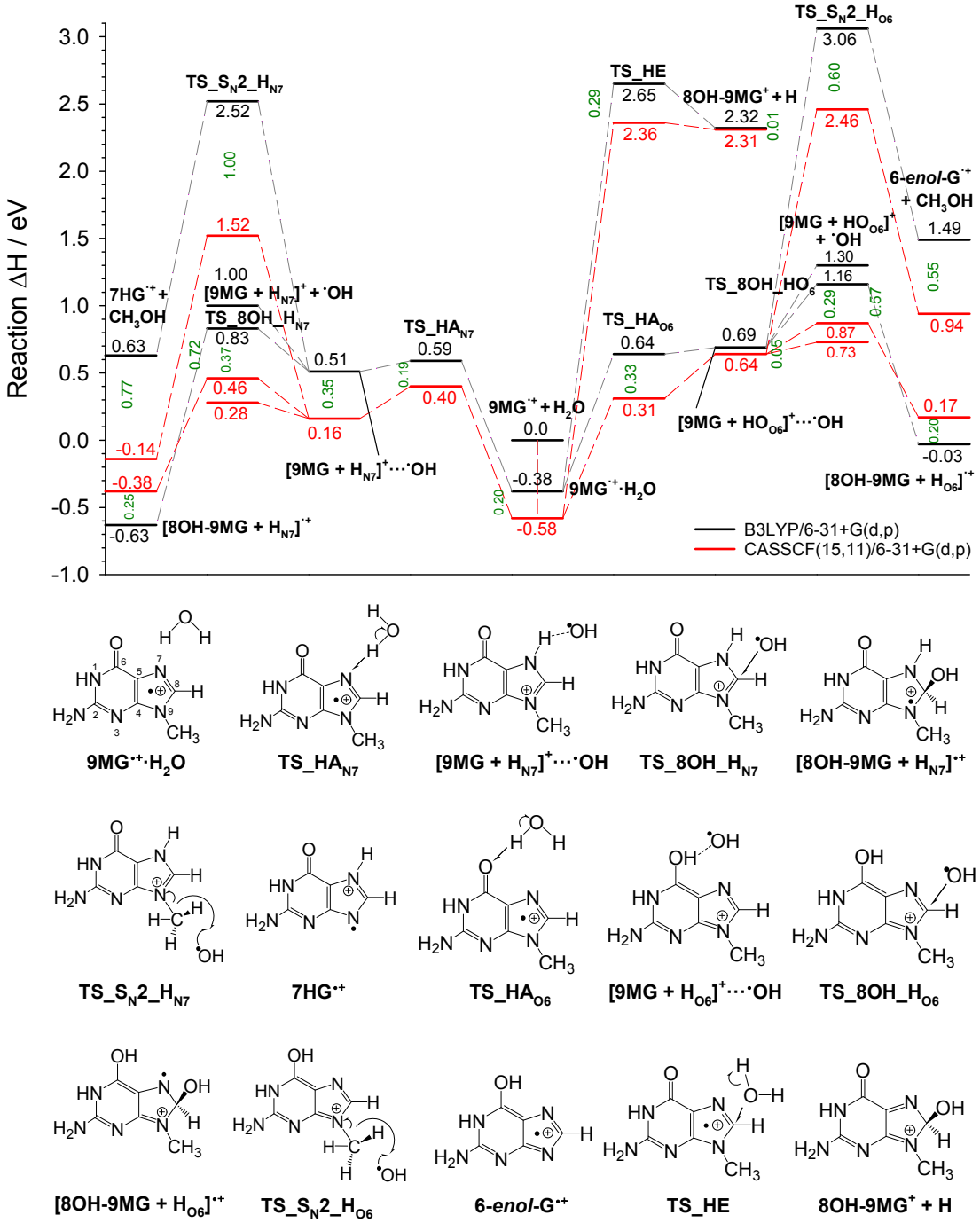
Reaction ΔH / eV
3.0
2.5
2.0
1.5
1.0
0.5
0.0
-0.5
-1.0
7HG·+ + CH3OH
0.63
[8OH-9MG + HN7]·+
-0.63
TS_SN2_HN7
2.52
1.52
1.00
[9MG + HN7]+ + ·OH
TS_8OH_HN7
0.83
0.46
0.28
0.51
0.16
[9MG + HN7]+···OH
TS_HAN7
0.59
0.40
9MG·+ + H2O
0.0
-0.38
-0.58
9MG·+·H2O
TS_HE
2.65
2.36
8OH-9MG+ + H
2.32
2.31
TS_HAO6
0.64
0.31
[9MG + HO6]+···OH
0.69
0.64
TS_SN2_HO6
3.06
2.46
[9MG + HO6]+ + ·OH
1.30
1.16
TS_8OH_HO6
0.87
0.73
6-enol-G·+ + CH3OH
1.49
0.94
0.17
-0.03
[8OH-9MG + HO6]·+
B3LYP/6-31+G(d,p)
CASSCF(15,11)/6-31+G(d,p)
9MG·+·H2O
TS_HAN7
[9MG + HN7]+···OH
TS_8OH_HN7
[8OH-9MG + HN7]·+
TS_SN2_HN7
7HG·+
TS_HAO6
[9MG + HO6]+···OH
TS_8OH_HO6
[8OH-9MG + HO6]·+
TS_SN2_HO6
6-enol-G·+
TS_HE
8OH-9MG+ + H

Fig. 7

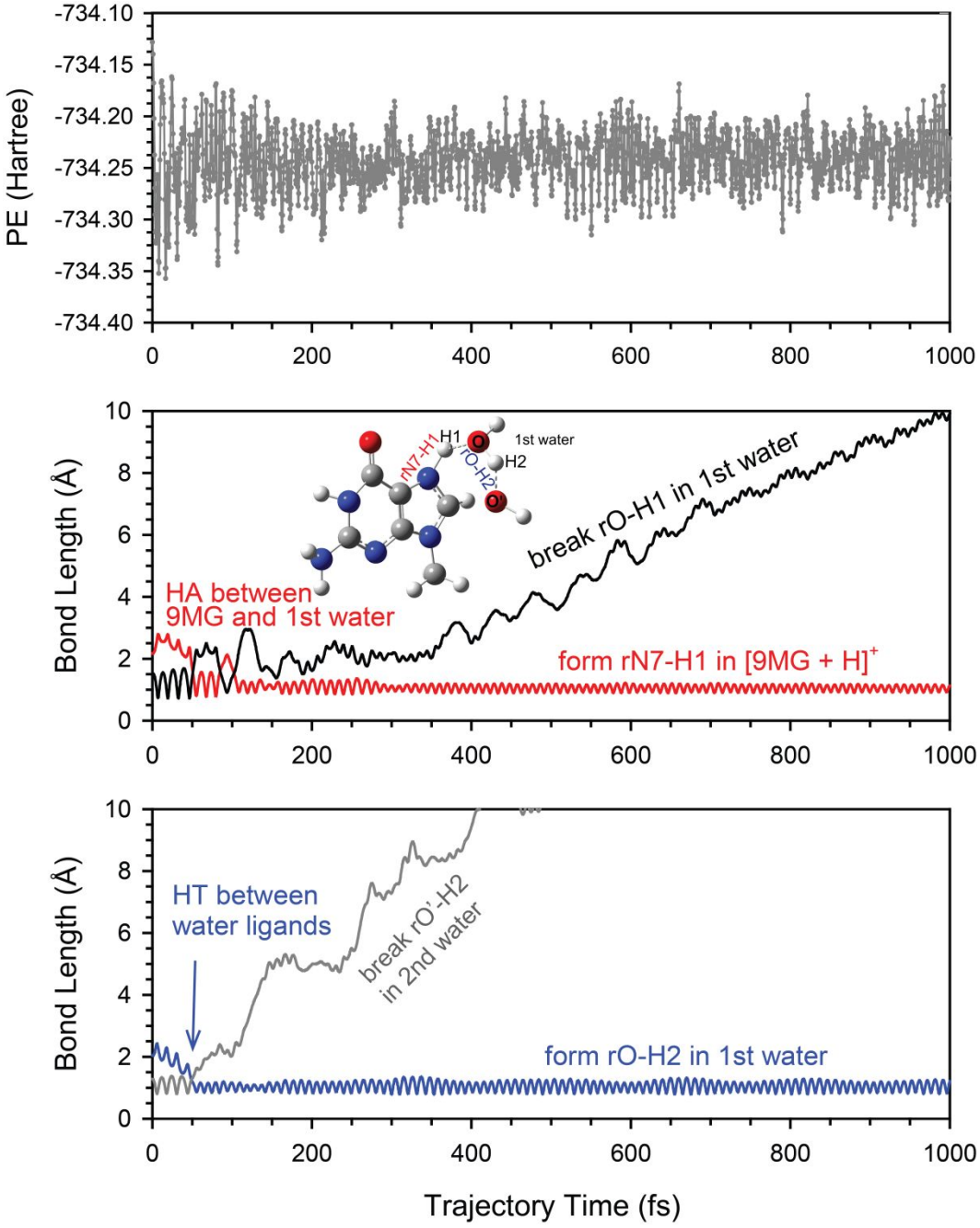
PE (Hartree)
-734.10
-734.15
-734.20
-734.25
-734.30
-734.35
-734.40
0
200
400
600
800
1000
Bond Length (Å)
rN7-H1
H1
1st water
rO-H2
H2
O'
break rO-H1 in 1st water
HA between
9MG and 1st water
form rN7-H1 in [9MG + H]+
HT between
water ligands
break rO'-H2
in 2nd water
form rO-H2 in 1st water
Trajectory Time (fs)

Fig. 8

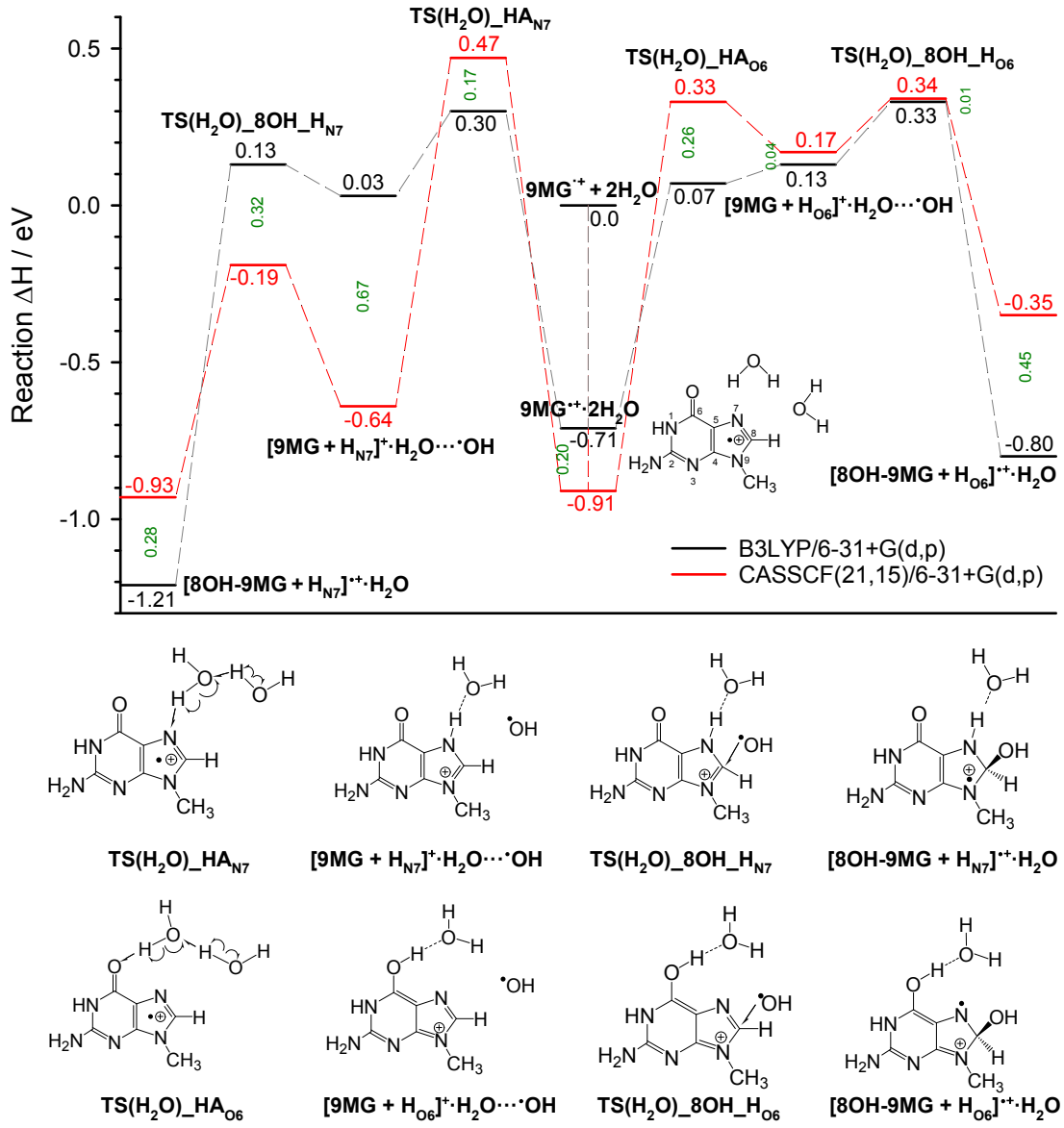
Reaction ΔH / eV
0.5
0.0
-0.5
-1.0
TS(H2O)_HAN7
0.47
TS(H2O)_8OH_HN7
0.13
0.03
0.30
0.17
0.32
0.67
-0.19
-0.64
[9MG + HN7]+·H2O···OH
-0.93
0.28
-1.21
[8OH-9MG + HN7]·+·H2O
9MG·+ + 2H2O
0.0
9MG·+·2H2O
-0.71
0.20
-0.91
TS(H2O)_HAO6
0.33
0.07
0.26
[9MG + HO6]+·H2O····OH
0.04
0.17
0.13
TS(H2O)_8OH_HO6
0.34
0.33
0.01
-0.35
0.45
-0.80
[8OH-9MG + HO6]·+·H2O
B3LYP/6-31+G(d,p)
CASSCF(21,15)/6-31+G(d,p)
TS(H2O)_HAN7
[9MG + HN7]+·H2O····OH
TS(H2O)_8OH_HN7
[8OH-9MG + HN7]·+·H2O
TS(H2O)_HAO6
[9MG + HO6]+·H2O····OH
TS(H2O)_8OH_HO6
[8OH-9MG + HO6]·+·H2O